Inverse design for material anisotropy and its application for a compact X-cut TFLN on-chip wavelength demultiplexer

Jiangbo Lyu, Tao Zhu, Yan Zhou, Zhenmin Chen, Yazhi Pi, Zhengtong Liu, Xiaochuan Xu, Ke Xu, Xu Ma, Lei Wang, Zizheng Cao and Shaohua Yu

---

Related articles

Spatio-temporal isolator in lithium niobate on insulator
Haijin Huang, Armandas Balčytis, Aditya Dubey, Andreas Boes, Thach G. Nguyen, Guanghui Ren, Mengxi Tan, Arnan Mitchell
Opto-Electronic Science   2023 **2**, 220022   doi: 10.29026/oes.2023.220022

Benchmarking deep learning-based models on nanophotonic inverse design problems
Taigao Ma, Mustafa Tobah, Haozhu Wang, L. Jay Guo
Opto-Electronic Science   2022 **1**, 210012   doi: 10.29026/oes.2022.210012

Chiral detection of biomolecules based on reinforcement learning
Yuxiang Chen, Fengyu Zhang, Zhibo Dang, Xiao He, Chunxiong Luo, Zhengchang Liu, Pu Peng, Yuchen Dai, Yijing Huang, Yu Li, Zheyu Fang
Opto-Electronic Science   2023 **2**, 220019   doi: 10.29026/oes.2023.220019

Intelligent metaphotonics empowered by machine learning
Sergey Krasikov, Aaron Tranter, Andrey Bogdanov, Yuri Kivshar
Opto-Electronic Advances   2022 **5**, 210147   doi: 10.29026/oea.2022.210147

More related article in Opto-Electron Journals Group website

Inverse design for material anisotropy and its application for a compact X-cut TFLN on-chip wavelength demultiplexer

Jiangbo Lyu[1,2†], Tao Zhu[1,2†], Yan Zhou[1], Zhenmin Chen[1], Yazhi Pi[1], Zhengtong Liu[1], Xiaochuan Xu[2], Ke Xu[2]*, Xu Ma[3]*, Lei Wang[1]*, Zizheng Cao[1]* and Shaohua Yu[1]

Inverse design focuses on identifying photonic structures to optimize the performance of photonic devices. Conventional scalar-based inverse design approaches are insufficient to design photonic devices of anisotropic materials such as lithium niobate (LN). To the best of our knowledge, this work proposes for the first time the inverse design method for anisotropic materials to optimize the structure of anisotropic-material based photonics devices. Specifically, the orientation dependent properties of anisotropic materials are included in the adjoint method, which provides a more precise prediction of light propagation within such materials. The proposed method is used to design ultra-compact wavelength division demultiplexers in the X-cut thin-film lithium niobate (TFLN) platform. By benchmarking the device performances of our method with those of classical scalar-based inverse design, we demonstrate that this method properly addresses the critical issue of material anisotropy in the X-cut TFLN platform. This proposed method fills the gap of inverse design of anisotropic materials based photonic devices, which finds prominent applications in TFLN platforms and other anisotropic-material based photonic integration platforms.

Keywords: integrated photonics; inverse design for anisotropic materials; adjoint method; lithium niobate

Introduction

Integrated photonics plays a key role in optical communications and on-chip optical interconnection, which consists of various photonics devices. Most traditional photonic integration devices are designed by analytical model-based approaches[1]. During the optimization process, the geometric shapes and material parameters of the photonic devices are usually given by a priori model and optimized by fine-tuning the individual characteristic parameters after several runs of numerical simulations[2], therefore the dimensionality of the traditional parametric optimization problem is limited[3]. In recent years, the

development of inverse design for photonics devices has overturned the situation[4−8]. Different from the traditional forward design approaches, inverse design method seeks the optimal parameter distribution of the photonics device structures in a larger parameter space through intelligent optimization algorithms, which consume fewer computing resources, bringing the performance of the designed photonic devices closer to their limits or the ideal states. Popular intelligent inverse design optimization algorithms include the adjoint method[9], genetic algorithm[10], particle swarm optimization[11], and neural network algorithm[12−15]. These algorithms have been applied to integrated photonic device design, for example, power division devices[16], wavelength division devices[17,18], gratings[19,20], and so on. Inverse design approaches generally focus on optimizing the spatial distribution of dielectric constants of photonic integrated devices for better performance while maintaining a small footprint. Currently, inverse design is widely used in the design of photonic integrated devices based on isotropic materials, including silicon-on-insulator (SOI)[21], Si₃N₄[22], and III-V compound semiconductors[23].

Owing to the CMOS-compatible fabrication process and excellent properties of LN, including strong optical confinement and large nonlinear susceptibility, the photonic devices based on thin-film lithium niobate (TFLN) have achieved rapid development[24]. Due to the anisotropy of lithium niobate materials, TFLN devices are usually divided into X-cut and Z-cut types. Within the past five years, different kinds of high-performance photonic integrated devices have been realized on the TFLN platform. Some notable works are summarized in a four-quadrant diagram below[25−42].

As shown in Fig. 1, the photonic integrated devices in the left half are based on the Z-cut TFLN designs, while those in the right half are based on the X-cut TFLN. From the lower to the upper half, representative LN integrated photonic devices based on traditional design methods and inverse design methods are displayed, respectively. It is obvious that fewer photonic devices are optimized by inverses design methods. One important reason is that previous inverse design methods cannot deal with the issue of X-cut TFLN anisotropy in the x/y plane. Currently, various X-cut TFLN devices are developed with traditional design methods, as seen in the fourth quadrant. Yet there are no previously published inverse design works for X-cut TFLN devices, as shown in the first quadrant. Although there are a few reports on

inverse design for Z-cut TFLN, the issue of material anisotropy is still not addressed. One of the key issues is that the dielectric constant in anisotropic materials is not a scalar identical in all directions as in the isotropic materials, but a tensor[43], which is typically represented by a 3×3 diagonal matrix, in which traditional scalar-based inverse design methods are no longer feasible.

Figure 2 briefly depicts the abovementioned X-cut type and Z-cut type of TFLN devices. Figure 2(a) presents a schematic diagram of the three-dimensional structure of X-cut TFLN waveguide, typically passive components are obtained using the wet etching process on the bonded wafers. Figure 2(b) depicts the refractive index ellipsoid of LN. It can be seen that the refractive index values are different along different crystal axes. Therefore, the spatially distributed dielectric constants are depicted as a 3×3 diagonal matrix, which is expressed as

$$\boldsymbol{\varepsilon} = \left[\begin{array}{ccc} \varepsilon_x & & \\ & \varepsilon_y & \\ & & \varepsilon_z \end{array} \right] , \qquad (1)$$

where $\varepsilon_x, \varepsilon_y$ and ε_z respectively represent dielectric constants along the x, y and z directions, and $\varepsilon_x = n_o^2$, $\varepsilon_y = n_o^2$ and $\varepsilon_z = n_e^2$. Figure 2(c) shows schematic diagrams of X-cut LN and Z-cut LN. It is noted that when light travels along the y/z plane in an X-cut TFLN device, it encounters two different refractive indices, which is not the case for the Z-cut TFLN devices. As a result, the traditional scalar-based inverse design methods can be applied to the Z-cut TFLN devices, but not to the X-cut ones.

Compared with Z-cut TFLN, X-cut TFLN modulators can make better use of electro-optic coefficient r_{33} to obtain higher modulation efficiency[44−46]. To enhance the capacity of the on-chip optical interconnection system, it is crucial for the system to separately modulate light within various wavelength bands. In this scenario, wavelength division demultiplexer devices play a pivotal role in this system. At present, there are two ways to integrate X-cut LN modulators with high modulation efficiency and passive components with other functions. One is to use hybrid integration technology to combine the X-cut TFLN modulator with inverse-designed compact passive devices made of isotropic materials[24,47−49]. This practice inevitably increases the fabrication complexity and incurs a higher optical power loss. The other way is to design passive components on the X-cut TFLN platform using traditional design methods, as such they can be fabricated on the same chip together with the
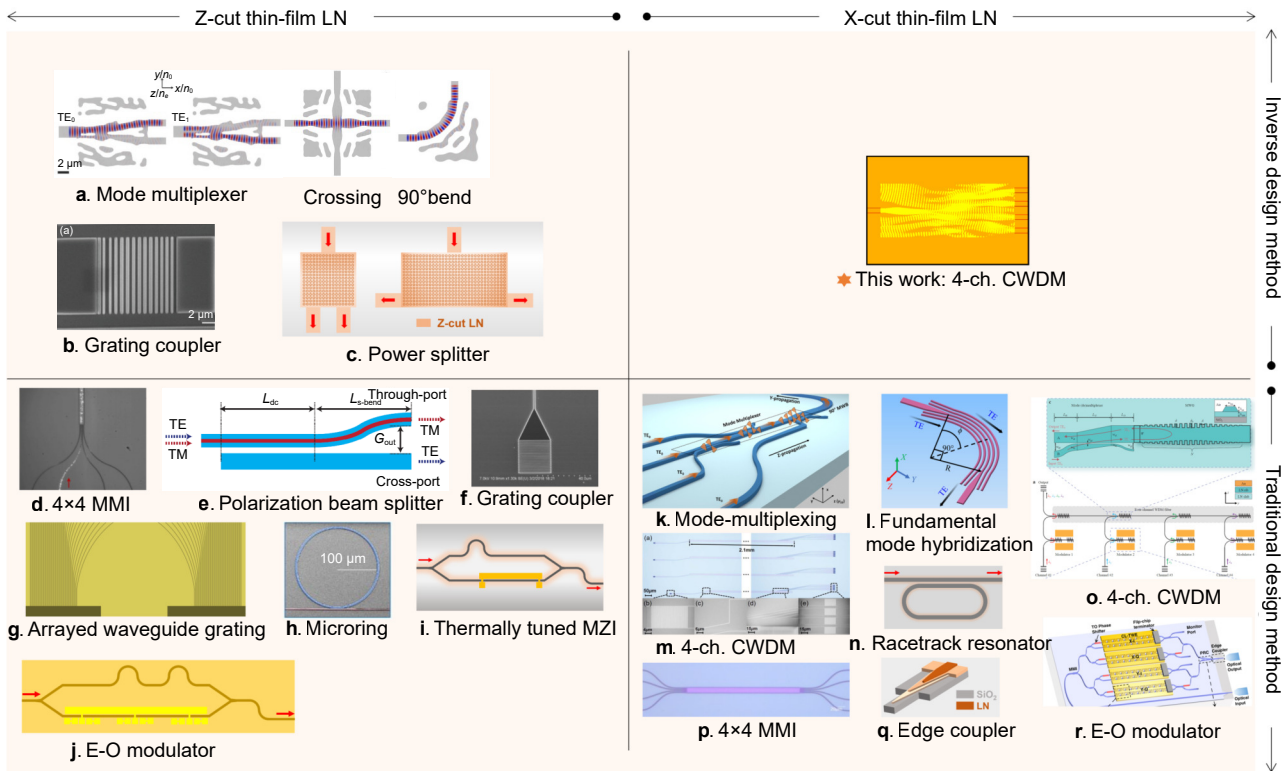
Fig. 1 | A four-quadrant diagram of photonics devices based on TFLN. (**a**) A spatial-mode multiplexer, a waveguide crossing, and a compact waveguide bend using a 3D gradient-based inverse-design method[25]. (**b**) A grating coupler using particle swarm optimization method[26]. (**c**) A power splitter using Direct binary search method[27]. (**d**) A 4×4 multimode interference (MMI)[28]. (**e**) A polarization beam splitter[29]. (**f**) An alignment-tolerant grating coupler[30]. (**g**) An arrayed waveguide grating[31]. (**h**) A microring resonator for soliton microcomb generation[32]. (**i**) A tunable Mach-Zehnder interferometer (MZI)[33]. (**j**) An integrated electro-optic modulator[34]. (**k**) A mode-multiplexing device[35]. (**l**) A fundamental mode hybridization[36]. (**m**) A 4 channel CWDM device[37]. (**n**) A compact racetrack resonator[38]. (**o**) A lithium niobate photonic chip for wavelength-division-multiplexing transmitters[39]. (**p**) A 4×4 MMI for C-band optical 90-degree hybrid[40]. (**q**) An ultra-broadband and low-loss edge coupler[41]. (**r**) A dual-polarization TFLN in-phase quadrature modulators[42]. Figure reproduced with permission from: (a) ref.[25], Copyright © 2023 American Chemical Society; (b) ref.[26], under a Creative Commons Attribution 4.0 International License; (d) ref.[28], Copyright © 2021 Optica Publishing Group; (e) ref.[29], under a Creative Commons Attribution 4.0 International License; (f) ref.[30], Copyright © 2019 Optica Publishing Group; (h) ref.[32], Copyright © 2019 Optica Publishing Group; (k) ref.[35], Copyright © 2023 John Wiley and Sons; (l) ref.[36], Copyright © 2023 Optica Publishing Group; (m) ref.[37], Copyright © 2022 Chinese Laser Press; (o) ref.[39], under a Creative Commons Attribution 4.0 International License; (p) ref.[40], Copyright © 2023 Optica Publishing Group; (r) ref.[42], Copyright © 2022 Optica Publishing Group.
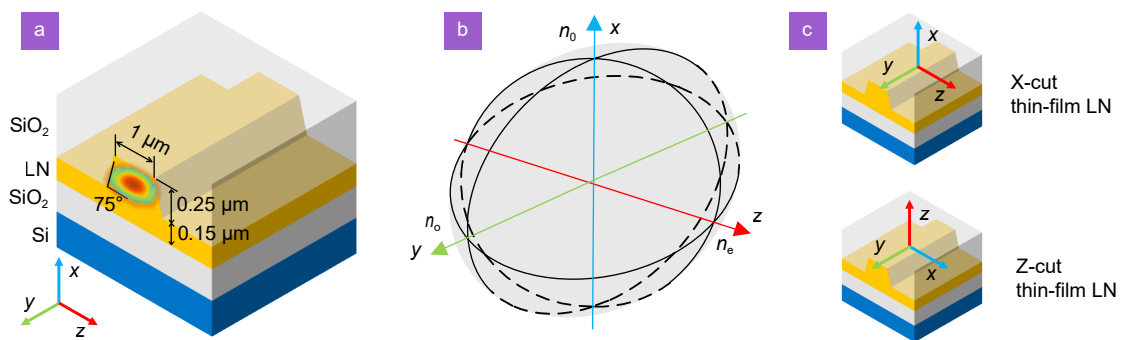

Fig. 2 | (**a**) Schematic diagram of the three-dimensional structure of X-cut LN waveguide. (**b**) Schematic diagram of refractive index ellipsoid. (**c**) Schematic diagram of X-cut LN and Z-cut LN.

modulator. This reduces the processing costs but does not reduce the footprint of the devices. It is desirable to extend the inverse design for X-cut TFLN passive devices.

In this paper, to the best of our knowledge, we report for the first time an inverse design method taking into account optically anisotropic materials and demonstrate its application in designing an ultra-compact TFLN wavelength division demultiplexer device. The implementation of photonics device simulation in the finite-difference time-domain (FDTD) method is achieved by separately handling the three-order diagonal matrix elements of the X-cut TFLN. To validate our approach, we conduct numerical simulations of the wavelength division demultiplexer. The incompatibility of the scalar-based inverse design method on anisotropic X-cut TFLN devices is investigated. We demonstrate the competency of our proposed approach to inverse-designing X-cut TFLN devices, and benchmark their performances with those of isotropic Z-cut TFLN devices using the classical method. Additionally, accounting for dispersion in the waveguide, the device can achieve less crosstalk and lower insertion loss by altering the shape of the simulation area while maintaining the device footprint. This proposed method fills the gap of inverse design of anisotropic materials based photonic devices, which finds prominent applications in TFLN platforms and other anisotropic-material based photonic integration platforms.

Methods

The workflow of the proposed inverse design method is shown in Fig. 3. Figure 3(a) illustrates the workflow of the inverse design algorithm for anisotropic materials, with the dielectric constant tensor serving as a pivotal parameter in this process. After initializing the model, this tensor undergoes normalization. Subsequently, the normalized epsilon is input into the FDTD simulation with forward and adjoint simulation. During each iteration, both a forward simulation and an adjoint simulation are required. In this phase, adjustments to the normalized dielectric constant tensor are made based on the gradients magnitude until either the iteration upper limit is met or optimal results are achieved. During binarization, the Heaviside filter transforms the linear mapping into a step function. During the iteration process, there exists a criterion to determine the completion of binarization, known as 'discreteness'. Discreteness is determined based on the average value of all normalized dielectric constants in the optimization region. When the discreteness reaches the predefined threshold value, usually 0.999, the binarization process is regarded to be completed, implying that there are only waveguide dielectric constants and background dielectric constants within the optimization area. This leads to the final optimization outcome.

Currently, the topology optimization method is widely used in inverse design, which realizes the isotropic inverse design of photonics devices[50–52]. Generally, this method uses the spatial distribution of the dielectric constant as the object of optimization. By doing so, this method can lead to devices with better performances, because it can provide more optimization parameters by
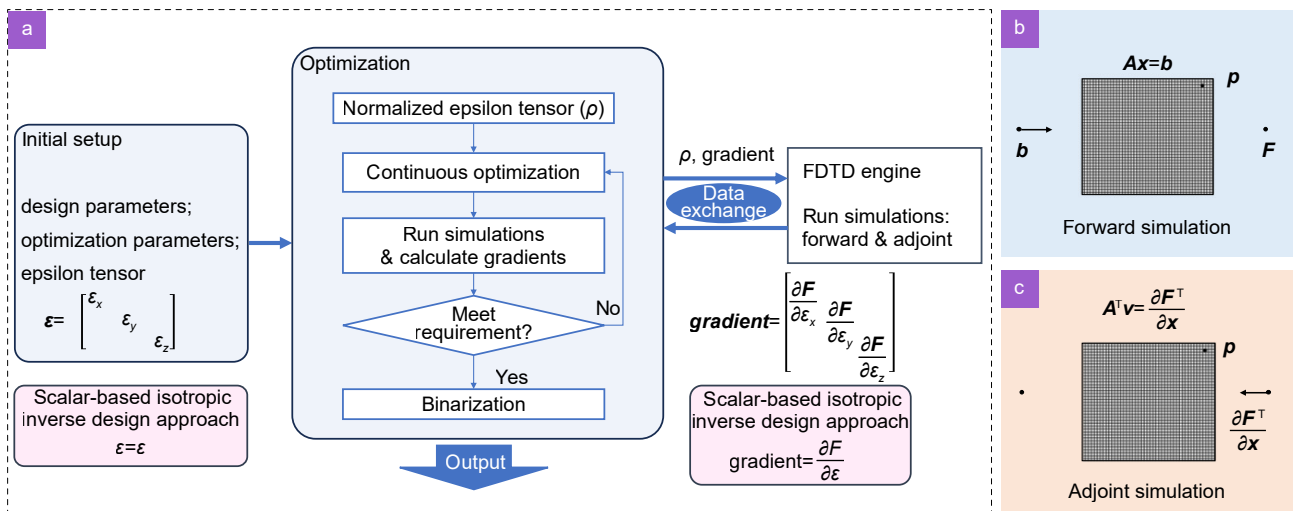
Fig. 3 | (a) Workflow of the inverse design method for anisotropic materials with the dielectric constant tensor. **(b)** Forward simulation of a linear system, **b** is a point source, **F** is the objective function at the measuring point, and **p** is the spatial distribution of the dielectric constant. **(c)** Adjoint simulation of a linear system, the point source given by $\partial F^{T}/\partial x$ is located at the measuring point.

virtue of greater degrees of freedom and larger design space. However, compared with the traditional design methods, topology optimization requires more computational resources and runtime.

To improve the computational efficiency, the adjoint method was introduced to the process of numerical simulation in topology optimization[53]. Compared with other intelligent optimization algorithms, this method can obtain the gradients of all design parameters in object function with two simulations, thus reducing computational complexity and resource consumption to a large extent, as shown in Fig. 3(b) and 3(c). A brief description of the adjoint method is as follows[53].

Assuming the system under consideration consists of linear materials, as shown in Fig. 3(b) and 3(c), the adjoint method requires two simulations to solve for the gradient of the objective function within the optimization region for the design variables. The Maxwell equations $R(x, p) = 0$ can be represented as Eq. (2).

$$Ax = b ,\qquad(2)$$

where A is the Maxwell operator, which can be formulated as $\begin{bmatrix} -\partial_t \varepsilon(t) * & \nabla \times \\ \nabla \times & \partial_t \mu \end{bmatrix}$; x represents the state variables, which might be the electric field E or magnetic field H, represented explicitly as $\begin{bmatrix} E \\ H \end{bmatrix}$; b is the source term, whether a current source J or a magnetic dipole M, with its particular form denoted as $\begin{bmatrix} J \\ -M \end{bmatrix}$.

The adjoint equation of the system can be represented as Eq. (3):

$$A^{\mathrm{T}} v = \left(\frac{\partial F}{\partial x}\right)^{\mathrm{T}} ,\qquad(3)$$

where v is the adjoint field; F is the objective function, depending on the state variable x and the design parameter p.

When simulating photonic devices with anisotropic materials, the spatial distribution of the dielectric constant is depicted as a diagonal matrix, which is expressed as Eq. (1). And the bold symbol represents the matrix form of the symbol.

In the adjoint method, the dielectric constant is calculated using the transpose of the diagonal matrix in Eq. (1), and A is represented as Eq. (4):

$$\begin{bmatrix} \varepsilon(-t)^{\mathrm{T}} * \partial_t & \nabla \times \\ \nabla \times & -\mu \partial_t \end{bmatrix} .\qquad(4)$$

The forward simulation and adjoint equation of the system are Eq. (5) and Eq. (6), respectively:

$$Ax = b ,\qquad(5)$$

$$A^{\mathrm{T}} v = \frac{\partial F^{\mathrm{T}}}{\partial x} .\qquad(6)$$

Therefore, the gradients of the target function for the design parameters can be expressed as Eq. (7):

$$\frac{\mathrm{d}F}{\mathrm{d}p} = \frac{\partial F}{\partial p_k} - v^{\mathrm{T}} \frac{\partial R}{\partial p_k} ,\qquad(7)$$

where p_k is k^{th} design parameter.

While the dielectric constant does not affect the computational complexity of FDTD simulation, the process of gradients calculation is different. Instead of a single element, it addresses three elements on the diagonal of a third-order matrix, tripling the computational complexity. In the scalar-based inverse design method, the Poynting vector and the wave vector are aligned. However, when anisotropic materials are involved, the Poynting vector and k direction are no longer parallel to each other in general[54,55]. Our proposed method effectively resolves the issue by introducing a third-order diagonal permittivity tensor of anisotropic materials in three-dimensional full-vector beam propagation method during the simulation.

Results and discussion

In this section, we demonstrate four types of wavelength division demultiplexers using the scalar-based inverse design method and the proposed inverse design method for anisotropic materials, respectively. The function of a wavelength division demultiplexer is to decompose the input composite optical signal into its constituent signals of individual wavelengths. These optical signals with different center wavelengths can then be separately processed or routed to different waveguides.

A four-channel wavelength division demultiplexer, working in the wavelength range of 1510 nm–1580 nm, is shown in Fig. 4(a). The left channel serves as the input channel of the broadband signal, and on the right are the four output channels. Ports 1, 2, 3, and 4 correspond to the wavelength ranges of 1510 nm–1520 nm, 1530 nm–1540 nm, 1550 nm–1560 nm, and 1570 nm–1580 nm, respectively. Each channel has a designed spectral width of 10 nm. Between each pair of neighboring channels, there is a 10 nm isolation in the wavelength spectrum and a physical spacing of 4 µm between adjacent waveguides. The refractive index of LN material is relatively small, which implies a weaker ability to refract light
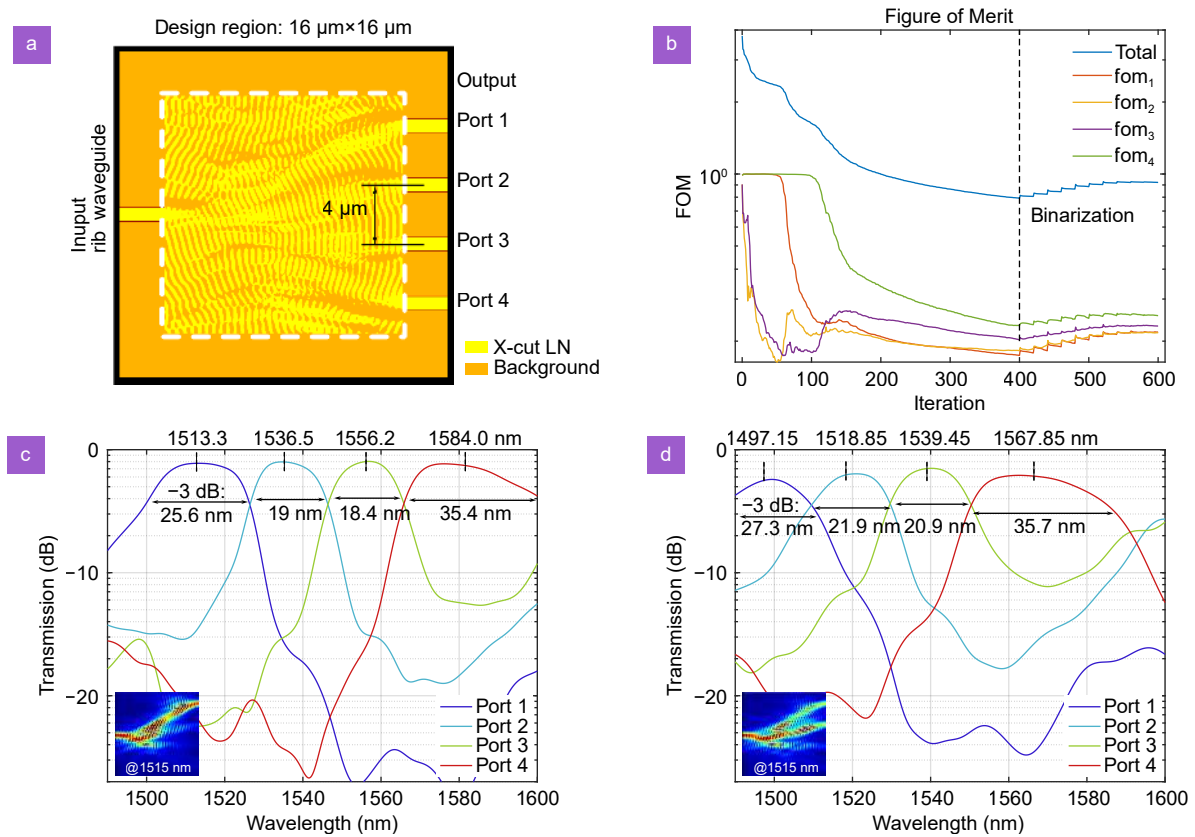
Fig. 4 | (a) Schematic of the inverse design of a thin-film LN four-channel wavelength division demultiplexer device. **(b)** The iterative process of FOM during the inverse design process, including the FOM for the four ports and the total FOM (blue line) of the device. **(c)** Spectral response of four output ports verified in FDTD simulation of a structure designed by inverse design using isotropic materials. Inset is the electric field distribution within the design region while the center wavelength of the input optical signal is 1515 nm. **(d)** Spectral response of four output ports verified in FDTD simulation of the same structure after setting the material of the structure to the tensor form of X-cut LN. Inset is the electric field distribution within the design region while the center wavelength of the input optical signal is 1515 nm.

as compared to silicon-based materials. As a result, wavelength division devices made of LN material tend to have larger dimensions than their silicon-based counterparts. In the initialization, the design area size is set to 16 μm × 16 μm. A slab waveguide is placed in the 16 μm × 16 μm design region with a thickness of 250 nm as the initial structure to allow light transmission from the input end to output ends. The mesh size is set to 50 nm and the minimum feature size is set to 200 nm in both the scalar-based inverse design method and the proposed inverse design method for anisotropic materials. Besides, four frequency monitors are set as figures of merit (FOMs) over the four output ports, which decrease and converge to a fixed value as the iteration number increases. It should be noted these simulation settings are applied throughout this manuscript.

In the scalar-based inverse design process, the targeted values of refractive index in the design area are optimized between the waveguide refractive index and the

cladding refractive index and eventually binarized. We first set the upper and lower limiting refractive index values to 2.21 and 1.44, respectively, because the refractive index of LN material in TE mode is 2.21[51]. We then set the target transmittance of the TE mode optical signal as 1 for each port. Here the FOM is the power coupling of guided modes[56], as shown in the equation below:

$$F = \left(\frac{1}{\lambda_2 - \lambda_1} \int_{\lambda_1}^{\lambda_2} |T_0(\lambda)|^L d\lambda \right)^{1/L}$$
$$- \left(\frac{1}{\lambda_2 - \lambda_1} \int_{\lambda_1}^{\lambda_2} |T(\lambda) - T_0(\lambda)|^L d\lambda \right)^{1/L}, \quad (8)$$

where T_0 is the forward transmission of the target light; λ_1 and λ_2 are the lower and upper limits of the wavelength points; T is the actual mode expansion power transmission; and L is the value of the generalized p-norm.

During the optimization, the overall FOM can be calculated as follows:

$$FOM = fom_1 + fom_2 + fom_3 + fom_4, \qquad (9)$$

where fom_i represents the transmittance of each port.

We first obtain an optimized demultiplexer device using traditional inverse design methods, as shown in Fig. 4. During optimization process, the FOMs of ports 2 and 3 drop quickly while FOMs of ports 1 and 4 stays the same. After some iterations, the FOMs of 1 and 4 start to drops. This phenomenon relates to the property of adjoint method. Specific explanations and intermediate processes can be found in the Supplementary information. After 400 steps of optimizations and 200 steps of binarizations, the FOM tends to be stable, and the final values of the four ports are 0.7749, 0.7954, 0.8028, and 0.7672, respectively. Subsequently, we extract the calculated structure and export the GDSII file (refer to Supplementary information) to perform another FDTD simulation for verification. In the verification simulation, we set the refractive index of the inverse design structure to 2.21. As seen in Fig. 4(c), results show that the spectral responses of the four output ports meet the design expectation. Optical signals of different wavelengths are guided to four ports, and the crosstalk between the ports is smaller than −11 dB. The output optical signals of the four ports are spectrally spaced at about 20 nm, and the four ports demonstrate −3 dB bandwidths of 25.6 nm, 19 nm, 18.4 nm, and 35.4 nm, respectively. This is because the total energy of all bands is limited, which imposes constraints on the spectral energy values of Ports 2 and 3 when dividing wavelengths. As a result, the −3 dB bandwidths obtained by Ports 2 and 3 are close to the designed value. In this wavelength division demultiplexer, there are no corresponding restrictions on the wavelength range outside the separation of Port 1 and Port 4. This leads to a much larger bandwidth than the designed parameter.

However, in practice, the refractive index of X-cut LN is not a single value. We replace the refractive index with a tensor form and conduct another verification simulation with the FDTD solver. As shown in Fig. 4(d), unsurprisingly, the results turned out to be quite different and did not meet the design expectations. The overall transmission spectrum is blue-shifted such that output optical signal wavelengths from the ports of interest are not as expected. As can be seen from the electric field distribution diagram in Fig. 4(d), when the wavelength range of the input optical signal is 1510–1520 nm, a considerable part of the light energy propagates to the second port,

which is not desired. The crosstalk between the three ports on the right are −7.66 dB, −8.65 dB, −11.07 dB and −8.84 dB, respectively. Therefore, we can see that the scalar-based inverse design is not suitable for anisotropic material systems.

Therefore, we turn to using the proposed inverse design method for anisotropic materials, which calculates the gradients of dielectric constants in a tensor form during the iteration process. In each step of the calculation, the refractive index value at every position within the design region is determined through parameter passing. These parameters are stored in matrix form. By doing so, the anisotropic material is taken into account in the optimization process, while the complexity of the FDTD simulation is not increased.

As we can see from Fig. 5(a), after 400 iterations and 200 binarizations, the FOM tends to level off and no longer changes. We extract the calculated structure to the GDSII file (refer to Supplementary information), set the material to X-cut LN, and perform a verification FDTD simulation, and the result is shown in Fig. 5(b). Since refractive indices of LN materials in the z-axis direction are relatively small, the transmission of each port is about 10% less than that of structures inverse-designed with isotropic materials in the same design region, and the crosstalk values between the ports are −11.96 dB, −11.96 dB, −11.69 dB, and −9.32 dB, respectively. Figure 5(c) visually shows that input optical signals in different wavelength ranges are propagated to their respective output ports, indicating that the device meets the design requirement. Figure 5(d) presents structural diagrams from two inverse design methods: the left depicts a device using the scalar-based inverse design method, while the right illustrates the one using the proposed inverse design method for anisotropic materials. Notably, the structures derived from these two inverse design methods are prominently different from each other. When compared with the X-cut wavelength division demultiplexer shown in Fig. 3(d), there is a marked improvement in the performance of the four ports. This reveals the significant impact of anisotropic materials in the inverse design of photonic devices.

Moreover, we modify the initial design region from a square to a rectangle, and we also used both methods to design a 25 μm×10 μm wavelength division demultiplexer. For the X-cut TFLN device, results using the proposed method are shown in Fig. 6, and results using the scalar-based inverse design method are displayed in
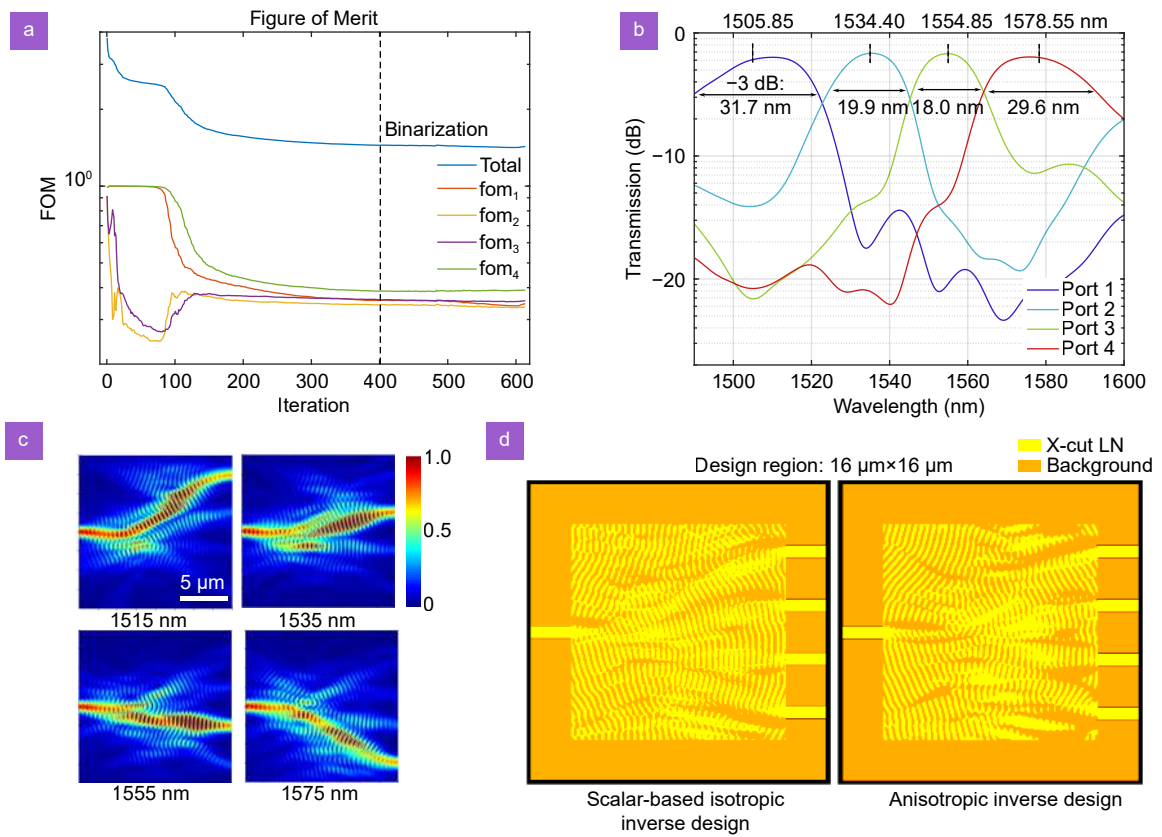
Fig. 5 | (**a**) The iterative process of FOM during the inverse design process using anisotropic materials, including the FOM for the four ports and the total FOM (blue) of the device. (**b**) Spectral response of four output ports verified in FDTD simulation of a structure designed by inverse design using anisotropic materials. (**c**) The electric field distribution within the design region while the center wavelengths of the input optical signal are 1515 nm, 1535 nm, 1555 nm, and 1575 nm, respectively. (**d**) The device structure designed using the scalar-based and the proposed inverse design methods for anisotropic materials, respectively.
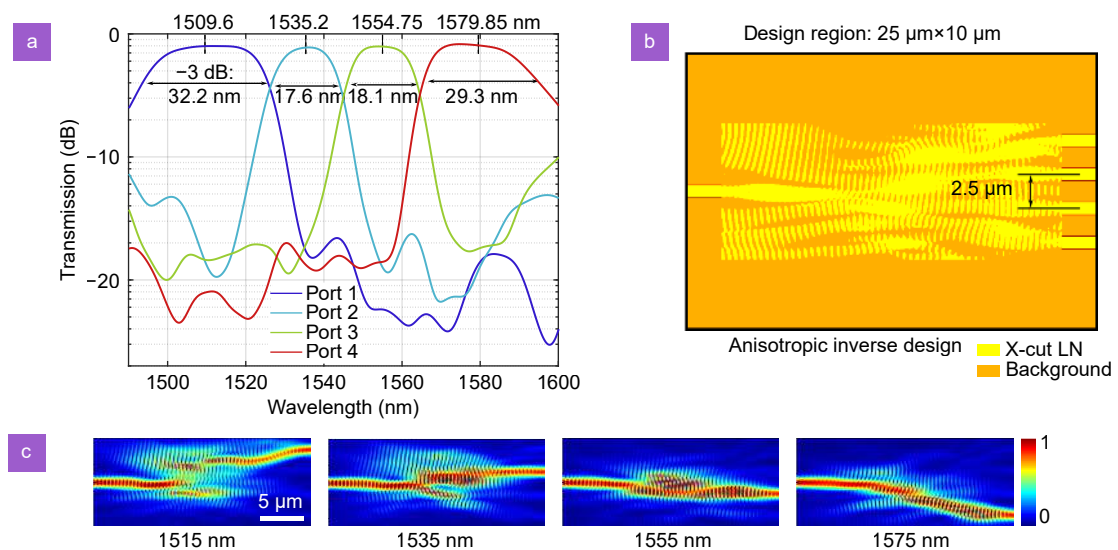

Fig. 6 | (**a**) Spectral response of four output ports verified in FDTD simulation. (**b**) The device structure with an initial design region of 25 μm×10 μm. (**c**) Electric field distributions within the design region for center wavelengths of the input optical signal at 1515 nm, 1535 nm, 1555 nm, and 1575 nm, respectively.

Fig. S2(b). In our design, we consider optimizing the performance of the device within the comparable device footprint. Under this circumstance, the average optical power output of each port has increased by nearly 1 dB, and the crosstalk of four ports are decreased to −17.4 dB, −16.1 dB, −17.5 dB, and −16.5 dB, respectively. Besides, the −3 dB bandwidths of four channels are 32.2 nm, 17.6 nm, 18.1 nm, and 29.3 nm, respectively. These results show that traditional scalar-based inverse design method is not suitable for anisotropic materials e.g., X-cut TFLN. Furthermore, the performances of the X-cut TFLN devices designed by our proposed inverse design method are comparable to those of the Z-cut devices designed by traditional method, which are detailed in Fig. S2(a). The elongated length of the device along the propagation direction amplifies the effect of dispersion in the waveguide, which is more advantageous for the device to realize wavelength division multiplexing and demultiplexing. Such a rectangular structure is more similar to the traditional MMI design structure. Simulation results indicate that the shape of the initial design region can influence the optimization results.

A comparison of device performances for the two inverse design methods is summarized in Table 1.

As shown in Table 1, wavelength division demultiplexers using the inverse design method for anisotropic materials have a better uniformity for −3 dB bandwidth, center wavelength deviance ($\Delta\lambda$) and insertion loss. Notably, the elongated design device possesses significantly smaller crosstalk values in all ports. On the contrary, the X-cut TFLN device obtained by the scalar-based inverse design method possesses inferior performances on these indicators.

In addition, we compare the performance of the wavelength division demultiplexers obtained by the proposed anisotropic method with those designed by the traditional intuition-based method, as shown in Table 2. As a comparison, the device designed by our proposed method has a prominently 3000 times smaller footprint. The smaller physical intervals between adjacent ports contribute to the larger crosstalk in our designed device.

Conclusions

In this work, we propose a novel inverse design method for photonics devices made of anisotropic materials. Using this method, we design two 1×4 wavelength division demultiplexers. By comparing with the scalar-based inverse design approach, we prove the effectiveness of the

Table 1 | Performance comparison of two inverse design methods.

Methods	Dimension	Port	−3 dB bandwidth	$\Delta\lambda$	Insertion loss	Crosstalk
Scalar-based inverse design	16 μm × 16 μm	1	27.3 nm	−17.80 nm	2.44 dB	−7.66 dB
		2	21.9 nm	−16.10 nm	2.04 dB	−8.66 dB
		3	20.9 nm	−15.50 nm	1.52 dB	−11.07 dB
		4	35.7 nm	−7.10 nm	2.10 dB	−8.85 dB
Our proposed method	16 μm × 16 μm	1	31.7 nm	−9.15 nm	2.02 dB	−11.96 dB
		2	19.9 nm	−0.60 nm	1.69 dB	−11.96 dB
		3	18.0 nm	0.15 nm	1.73 dB	−11.69 dB
		4	29.6 nm	3.55 nm	1.99 dB	−9.32 dB
Scalar-based inverse design	25 μm × 10 μm	1	18.6 nm	−17.85 nm	1.99 dB	−12.33 dB
		2	17.5 nm	−17.15 nm	1.68 dB	−9.39 dB
		3	20.8 nm	−19.00 nm	1.60 dB	−11.33 dB
		4	36.8 nm	−9.7 nm	0.96 dB	−15.11 dB
Our proposed method	25 μm × 10 μm	1	32.2 nm	−5.40 nm	0.97 dB	−17.40 dB
		2	17.6 nm	0.20 nm	1.08 dB	−16.10 dB
		3	18.1 nm	−0.25 nm	1.00 dB	−17.50 dB
		4	29.3 nm	4.85 nm	0.82 dB	−16.50 dB

Table 2 | Performance comparison of devices between metamaterial-assisted intuition-based method and anisotropic inverse design.

Method	Dimension	Channels	Bandwidth	Insertion loss	Crosstalk	Reference
Model-based method	2100 μm × 20 μm	4	12.1 nm (−3 dB)	0.72 dB	−18.0 dB	37
Model-based method	2800 μm × 300 μm	4	16.5 nm (−1 dB)	0.80 dB	−22 dB	39
Our proposed method	25 μm × 10 μm	4	17.6 nm (−3 dB)	1.08 dB	−16.1 dB	This work

proposed inverse design method for anisotropic materials. It should be noted that we do not take the impact of fabrication errors into account, and this method inevitably demands a computational complexity three times greater than the traditional scalar-based approach in the process of data processing. Besides being applied to LN-based material, this novel approach can also be extended to other optically anisotropic materials with enhanced simulation accuracies. It not only provides a more precise prediction of light propagation within these materials in FDTD simulations, but also ensures optimal performance of designed devices to a large extent. This method fills the gap of inverse design in anisotropic materials and lays a solid foundation for the development of anisotropic optoelectronic and photonic devices. Moreover, photonics devices developed using this method might play a significant part in photonic integrated circuits in the future.

References

1. Koenderink AF, Alù A, Polman A. Nanophotonics: shrinking light-based technology. *Science* **348**, 516–521 (2015).
2. Liu ZC, Zhu DY, Raju L, Cai WS. Tackling photonic inverse design with machine learning. *Adv Sci* **8**, 2002923 (2021).
3. Molesky S, Lin ZN, Piggott AY, Jin WL, Vucković J et al. Inverse design in nanophotonics. *Nat Photonics* **12**, 659–670 (2018).
4. Callewaert F, Velev V, Kumar P, Sahakian AV, Aydin K. Inverse-designed broadband all-dielectric electromagnetic metadevices. *Sci Rep* **8**, 1358 (2018).
5. Su LG, Trivedi R, Sapra NV, Piggott AY, Vercruysse D et al. Fully-automated optimization of grating couplers. *Opt Express* **26**, 4023–4034 (2018).
6. Lin CH, Chen YS, Lin JT, Wu HC, Kuo HT et al. Automatic inverse design of high-performance beam-steering metasurfaces via genetic-type tree optimization. *Nano Lett* **21**, 4981–4989 (2021).
7. Feichtner T, Selig O, Kiunke M, Hecht B. Evolutionary optimization of optical antennas. *Phys Rev Lett* **109**, 127701 (2012).
8. Qi HX, Du ZC, Hu XY, Yang JY, Chu SS et al. High performance integrated photonic circuit based on inverse design method. *Opto-Electron Adv* **5**, 210061 (2022).
9. Hughes TW, Minkov M, Williamson IAD, Fan SH. Adjoint method and inverse design for nonlinear nanophotonic devices. *ACS Photonics* **5**, 4781–4787 (2018).
10. Liu JC, Zhang D, Yu DQ, Ren MX, Xu JJ. Machine learning powered ellipsometry. *Light Sci Appl* **10**, 55 (2021).
11. Paganini A, Sargheini S, Hiptmair R, Hafner C. Shape optimization of microlenses. *Opt Express* **23**, 13099–13107 (2015).
12. Zhu RC, Qiu TS, Wang JF, Sui S, Hao CL et al. Phase-to-pattern inverse design paradigm for fast realization of functional metasurfaces via transfer learning. *Nat Commun* **12**, 2974 (2021).
13. Jiang JQ, Fan JA. Global optimization of dielectric metasurfaces using a physics-driven neural network. *Nano Lett* **19**, 5366–5372 (2019).
14. Krasikov S, Tranter A, Bogdanov A, Kivshar Y. Intelligent metaphotonics empowered by machine learning. *Opto-Electron Adv* **5**, 210147 (2022).
15. Ma TG, Tobah M, Wang HZ, Guo LJ. Benchmarking deep learning-based models on nanophotonic inverse design problems. *Opto-Electron Sci* **1**, 210012 (2022).
16. Zhou M, Liu DJ, Belling SW, Cheng HT, Kats MA et al. Inverse design of metasurfaces based on coupled-mode theory and adjoint optimization. *ACS Photonics* **8**, 2265–2273 (2021).
17. Sell D, Yang JJ, Doshay S, Yang R, Fan JA. Large-angle, multifunctional metagratings based on freeform multimode geometries. *Nano Lett* **17**, 3752–3757 (2017).
18. Piggott AY, Lu J, Lagoudakis KG, Petykiewicz J, Babinec TM et al. Inverse design and demonstration of a compact and broadband on-chip wavelength demultiplexer. *Nat Photonics* **9**, 374–377 (2015).
19. Fan LJ, Mei J. Acoustic metagrating circulators: nonreciprocal, robust, and tunable manipulation with unitary efficiency. *Phys Rev Appl* **15**, 064002 (2021).
20. Sell D, Yang JJ, Wang EW, Phan T, Doshay S et al. Ultra-high-efficiency anomalous refraction with dielectric metasurfaces. *ACS Photonics* **5**, 2402–2407 (2018).
21. Dai DX. Advanced passive silicon photonic devices with asymmetric waveguide structures. *Proc IEEE* **106**, 2117–2143 (2018).
22. Bayati E, Pestourie R, Colburn S, Lin ZN, Johnson SG et al. Inverse designed metalenses with extended depth of focus. *ACS Photonics* **7**, 873–878 (2020).
23. Ramirez JM, Elfaiki H, Verolet T, Besancon C, Gallet A et al. III-V-on-silicon integration: from hybrid devices to heterogeneous photonic integrated circuits. *IEEE J Sel Top Quantum Electron* **26**, 6100213 (2020).
24. Zhu D, Shao LB, Yu MJ, Cheng R, Desiatov B et al. Integrated photonics on thin-film lithium niobate. *Adv Opt Photonics* **13**, 242–352 (2021).
25. Shang CF, Yang JW, Hammond AM, Chen ZX, Chen M et al. Inverse-designed lithium niobate nanophotonics. *ACS Photonics* **10**, 1019–1026 (2023).
26. Xie YJ, Nie MM, Huang SW. Inverse-designed broadband low-loss grating coupler on thick lithium-niobate-on-insulator platform. arXiv: 2309.12976 (2023).
   https://doi.org/10.48550/arXiv.2309.12976
27. Xu Q, Liu JM, Zhang DL, Hua PR. Ultra-compact lithium niobate power splitters designed by an intelligent algorithm. *Opt Laser Technol* **160**, 109057 (2023).
28. Chen GY, Ng JD, Lin HL, Zhang G, Gong X et al. Design and fabrication of high-performance multimode interferometer in lithium niobate thin film. *Opt Express* **29**, 15689–15698 (2021).
29. Zhang L, Zhang L, Fu X, Yang L. Compact, broadband and low-loss polarization beam splitter on lithium-niobate-on-insulator using a silicon nanowire assisted waveguide. *IEEE Photonics J* **12**, 6601906 (2020).
30. Kar A, Bahadori M, Gong SB, Goddard LL. Realization of alignment-tolerant grating couplers for z-cut thin-film lithium niobate. *Opt Express* **27**, 15856–15867 (2019).
31. Tu HL, Zhang YD, Guo WH. Arrayed waveguide grating based on z-cut lithium niobate platform. In *2023 Opto-Electronics and Communications Conference (OECC)* 1–3 (IEEE, 2023);
   http://doi.org/10.1109/OECC56963.2023.10209708.

32. Gong Z, Liu XW, Xu YT, Xu MR, Surya JB et al. Soliton micro-comb generation at 2 μm in z-cut lithium niobate microring resonators. *Opt Lett* **44**, 3182–3185 (2019).

33. Chen GY, Lin HL, Ng JD, Danner AJ. Integrated thermally tuned Mach-Zehnder interferometer in z-cut lithium niobate thin film. *IEEE Photonics Technol Lett* **33**, 664–667 (2021).

34. Chen GY, Lin HL, Ng JD, Danner AJ. Integrated electro-optic modulator in z-cut lithium niobate thin film with vertical structure. *IEEE Photonics Technol Lett* **33**, 1285–1288 (2021).

35. Zhao WK, Liu RR, Zhu MY, Guo ZH, He JH et al. High-performance mode-multiplexing device with anisotropic lithium-niobate-on-insulator waveguides. *Laser Photonics Rev* **17**, 2200774 (2023).

36. Zheng XX, Lin ZX, Huang QS, He SL. Elimination of the fundamental mode hybridization on an x-cut lithium-niobate-on-insulator by using a densely packed bent waveguide array. *Appl Opt* **62**, 5765–5771 (2023).

37. Chen GX, Ruan ZL, Wang Z, Huang PC, Guo CJ et al. Four-channel CWDM device on a thin-film lithium niobate platform using an angled multimode interferometer structure. *Photonics Res* **10**, 8–13 (2022).

38. Pan BC, Tan Y, Chen PX, Liu L, Shi YC et al. Compact racetrack resonator on LiNbO₃. *J Lightwave Technol* **39**, 1770–1776 (2021).

39. Liu HX, Pan BC, Huang YS, He JH, Zhang M et al. Ultra-compact lithium niobate photonic chip for high-capacity and energy-efficient wavelength-division-multiplexing transmitters. *Light Adv Manuf* **4**, 133–142 (2023).

40. Tan HY, Wang J, Ke W, Zhang X, Zhao ZK et al. C-Band optical 90-degree hybrid using thin film lithium niobate. *Opt Lett* **48**, 1946–1949 (2023).

41. Liu XY, Gao SQ, Zhang C, Pan Y, Ma R et al. Ultra-broadband and low-loss edge coupler for highly efficient second harmonic generation in thin-film lithium niobate. *Adv Photonics Nexus* **1**, 016001 (2022).

42. Xu MY, Zhu YT, Pittalà F, Tang J, He MB et al. Dual-polarization thin-film lithium niobate in-phase quadrature modulators for terabit-per-second transmission. *Optica* **9**, 61–62 (2022).

43. Halir R, Cheben P, Luque-González JM, Sarmiento-Merenguel JD, Schmid JH et al. Ultra-broadband nanophotonic beamsplitter using an anisotropic sub-wavelength metamaterial. *Laser Photonics Rev* **10**, 1039–1046 (2016).

44. Zhuang RJ, He JZ, Qi YF, Li Y. High-*Q* thin-film lithium niobate microrings fabricated with wet etching. *Adv Mater* **35**, 2208113 (2023).

45. Sun DH, Zhang YW, Wang DZ, Song W, Liu XY et al. Microstructure and domain engineering of lithium niobate crystal films

for integrated photonic applications. *Light Sci Appl* **9**, 197 (2020).

46. Rao A, Patil A, Rabiei P, Honardoost A, Desalvo R et al. High-performance and linear thin-film lithium niobate Mach–Zehnder modulators on silicon up to 50 GHz. *Opt Lett* **41**, 5700–5703 (2016).

47. He MB, Xu MY, Ren YX, Jian J, Ruan ZL et al. High-performance hybrid silicon and lithium niobate Mach–Zehnder modulators for 100 Gbit s⁻¹ and beyond. *Nat Photonics* **13**, 359–364 (2019).

48. Chen L, Xu Q, Wood MG, Reano RM. Hybrid silicon and lithium niobate electro-optical ring modulator. *Optica* **1**, 112–118 (2014).

49. Weigel PO, Zhao J, Fang K, Al-Rubaye H, Trotter D et al. Bonded thin film lithium niobate modulator on a silicon photonics platform exceeding 100 GHz 3-dB electrical modulation bandwidth. *Opt Express* **26**, 23728–23739 (2018).

50. Jensen JS, Sigmund O. Topology optimization for nano-photonics. *Laser Photonics Rev* **5**, 308–321 (2011).

51. Lin Z, Liu V, Pestourie R, Johnson SG. Topology optimization of freeform large-area metasurfaces. *Opt Express* **27**, 15765–15775 (2019).

52. Wang Q, Chumak AV, Pirro P. Inverse-design magnonic devices. *Nat Commun* **12**, 2636 (2021).

53. Boes A, Corcoran B, Chang L, Bowers J, Mitchell A. Status and potential of lithium niobate on insulator (LNOI) for photonic integrated circuits. *Laser Photonics Rev* **12**, 1700256 (2018).

54. Lee D, So S, Hu GW, Kim M, Badloe T et al. Hyperbolic metamaterials: fusing artificial structures to natural 2D materials. *eLight* **2**, 1 (2022).

55. Dai ZG, Hu GW, Si GY, Ou QD, Zhang Q et al. Edge-oriented and steerable hyperbolic polaritons in anisotropic van der Waals nanocavities. *Nat Commun* **11**, 6086 (2020).

56. Lalau-Keraly CM, Bhargava S, Miller OD, Yablonovitch E. Adjoint shape optimization applied to electromagnetic design. *Opt Express* **21**, 21693–21701 (2013).

Acknowledgements

Competing interests

The authors declare no competing financial interests.

Supplementary information

Supplementary information for this paper is available at
https://doi.org/10.29026/oes.2023.230038